phys. stat. sol. (b) **242**, No. 11, 2197–2209 (2005) / **DOI** 10.1002/pssb.200560970

Feature Article

Exciton-polaritons and nanoscale cavities in photonic crystal slabs

Lucio Claudio Andreani*, **Dario Gerace,** and **Mario Agio****

Dipartimento di Fisica "Alessandro Volta", Università di Pavia, via Bassi 6, 27100 Pavia, Italy

Received 6 May 2005, revised 30 June 2005, accepted 1 July 2005
Published online 3 August 2005

PACS 42.50.Ct, 42.70.Qs, 71.36.+c, 73.20.Mf, 78.20.Bh

Recent theoretical work on exciton–light coupling in waveguide-embedded photonic crystals is reviewed. After a short description of the theory of photonic crystal slabs, the following issues are discussed: (i) a quantum-mechanical formulation of the interaction between photonic modes and quantum-well excitons, leading to a description of photonic crystal polaritons; (ii) calculations of variable-angle reflectance spectra, which show that radiative polaritons can be excited by an optical beam incident on the slab surface; (iii) a description of nanoscale cavities with extremely high Q-factors and low mode volumes in photonic crystal slabs; (iv) a quantum-mechanical model of the interaction between confined nanocavity modes and single quantum-dot transitions, leading again to a strong-coupling regime of light–matter interaction.

© 2005 WILEY-VCH Verlag GmbH & Co. KGaA, Weinheim

1 Introduction

Strong exciton–light coupling and the formation of polariton states is a recurring theme in solid-state physics and optics. The quantum theory of exciton-polaritons in bulk crystals was first formulated by Hopfield [1] and Agranovich [2]. The effect of quantum confinement on exciton-polariton states has been the subject of a number of investigations (for reviews see, e.g., [3–5]). Photon confinement in planar semiconductor microcavities with embedded quantum wells (QWs) leads to a strong-coupling regime of exciton–light coupling and to robust cavity polariton states [6–9]. Exciton–light coupling in microcavities with full three-dimensional photon confinement, like micro-pillars and micro-disks, has also been investigated [10–12].

The field of photonic crystals (PhCs) has become increasingly important since the pioneering works of Yablonovitch [13] and John [14]. In particular, photonic crystals embedded in planar waveguides (also known as photonic crystal slabs) can lead to a full control of light propagation because of a two-dimensional (2D) photonic lattice in the slab plane combined with dielectric confinement in the vertical direction [15–17]. Nanoscale cavities in PhC slabs with extremely high Q-factors and low mode volumes have been recently demonstrated [18, 19]. The performance of these nanocavity structures for optical confinement is, in principle, much better than that of conventional planar microcavities or of micro-pillar and micro-disk structures. Recently, the strong-coupling regime of quantum dot transitions coupled to high-Q cavity modes has been demonstrated for both micro-pillars [20] and PhC nanocavities [21].

In this paper we describe recent theoretical work dealing with exciton-polariton states in PhCs and in nanocavities. In Section 2 we review a few basic concepts related to photonic mode dispersion in PhC

* Corresponding author: e-mail: andreani@fisicavolta.unipv.it, Phone: +39 0382 987 491, Fax: +39 0382 987 563
** Presently at: Physical Chemistry Laboratory, Swiss Federal Institute of Technology (ETH), CH-8093 Zürich, Switzerland

© 2005 WILEY-VCH Verlag GmbH & Co. KGaA, Weinheim

slabs. In Section 3 we present a quantum-mechanical formulation of exciton-light coupling in PhC slabs with embedded QWs, leading to the conditions for the occurrence of a strong-coupling regime, and calculations of variable-angle reflectance from the slab surface: the quantum and semiclassical approaches agree with each other and show that radiative exciton-polaritons can be probed by surface reflectivity. In Section 4 we describe a basic nanocavity structure and present results for the *Q*-factor as a function of cavity geometry. In Section 5 we treat the coupling of a single quantum-dot transition with a high-*Q* cavity mode, and quantify the conditions for the occurrence of a strong-coupling regime. Section 6 contains concluding remarks.

2 Mode dispersion and linewidths in photonic crystal slabs

Photonic crystal slabs consist of planar dielectric waveguides patterned with a one-dimensional (1D) or two-dimensional (2D) lattice. They can have either a weak refractive index contrast between core and claddings (like in the GaAs/AlGaAs or InP/InGaAsP systems) or a strong index contrast like in the self-standing membrane or air-bridge. Electromagnetic eigenmodes in PhC slabs can be either truly guided (if their frequency lies below the light line of the cladding material) or quasi-guided (if the frequency lies above the light line). Truly guided modes are evanescent in the cladding regions and have low propagation losses that are due only to fabrication disorder (in the transparency region of the medium in which absorption losses are absent). Quasi-guided modes, instead, have a radiative component in the cladding regions and suffer from high scattering losses due to diffraction out of the slab plane. For the same reason, however, they couple to an electromagnetic wave incident on the slab surface and represent optically active excitations of the photonic system. Indeed, the dispersion relations of quasi-guided modes have been studied in a number of angle-resolved linear [22–25] and nonlinear [26–29] experiments. Recently, truly-guided modes have also been probed by optical experiments from the slab surface using an attenuated-total-reflectance configuration [30].

In order to calculate the dispersion relations of guided and quasi-guided modes in PhC slabs, we adopt the guided-mode expansion (GME) method recently developed [31]. As conveniently done for photonic crystals, we start from the second-order equation for the magnetic field

$$\nabla\times\left[\frac{1}{\varepsilon(\boldsymbol{r})}\nabla\times\boldsymbol{H}\right]=\frac{\omega^2}{c^2}\boldsymbol{H}\,, \tag{1}$$

where $\varepsilon(\boldsymbol{r})$ is the spatially dependent dielectric constant. If the magnetic field is expanded in an orthonormal basis set as $\boldsymbol{H}(\boldsymbol{r})=\sum_\mu c_\mu \boldsymbol{H}_\mu(\boldsymbol{r})$, then Eq. (1) is transformed into a linear eigenvalue problem

$$\sum_\nu \mathcal{H}_{\mu\nu}c_\nu=\frac{\omega^2}{c^2}c_\mu\,, \tag{2}$$

where the matrix $\mathcal{H}_{\mu\nu}$ (which is the analog of a quantum Hamiltonian) is given by

$$\mathcal{H}_{\mu\nu}=\int\frac{1}{\varepsilon(\boldsymbol{r})}(\nabla\times\boldsymbol{H}^*_\mu(\boldsymbol{r}))\cdot(\nabla\times\boldsymbol{H}_\nu(\boldsymbol{r}))\,\mathrm{d}\boldsymbol{r}\,. \tag{3}$$

For the case of a PhC slab we have a waveguide along *z* and a periodic patterning in the xy plane. The basis states $\boldsymbol{H}_\mu(\boldsymbol{r})$ are chosen to consist of the guided modes of an effective waveguide, where each layer j has a homogeneous dielectric constant given by the spatial average of $\varepsilon_j(x,y)$. The index μ can be written as $\mu=(\boldsymbol{k}+\boldsymbol{G},\alpha)$, where $\boldsymbol{k}$ is the 2D Bloch vector, $\boldsymbol{G}$ is a reciprocal lattice vector and α labels the guided modes at wave vector $\boldsymbol{k}+\boldsymbol{G}$. The basis states with the same Bloch vector $\boldsymbol{k}$ are coupled by the dielectric modulation. The matrix elements (3) can be expressed in terms of the inverse dielectric tensor in each layer $\varepsilon_j^{-1}(\boldsymbol{G},\boldsymbol{G}')$, which is evaluated by a numerical inversion of the dielectric matrix $\varepsilon_j(\boldsymbol{G},\boldsymbol{G}')$.

© 2005 WILEY-VCH Verlag GmbH & Co. KGaA, Weinheim

The basis set consisting of the guided modes of the effective waveguide is orthonormal but not complete since the leaky modes of the waveguide are not included. Coupling to leaky modes produces a second-order shift of the mode frequency: the neglect of this effect (which is usually small, at least for the low air fractions that are employed here) is the main approximation of the method. When the guided modes are folded in the first Brillouin zone, many of them fall above the light line and become quasi-guided. Indeed, first-order coupling to leaky modes at the same frequency leads to a radiative decay width, which is expressed as twice an imaginary part of the frequency. This can be calculated by time-dependent perturbation theory, like in Fermi Golden Rule for quantum mechanics, and is given by

$$-\mathrm{Im}\left(\frac{\omega_{\boldsymbol{k}}^2}{c^2}\right) = \pi\left|\mathcal{H}_{\text{leaky, guided}}\right|^2 \rho\left(\boldsymbol{k};\frac{\omega_{\boldsymbol{k}}^2}{c^2}\right), \tag{4}$$

where $\rho(\boldsymbol{k};\omega_{\boldsymbol{k}}^2/c^2)$ is the 1D photonic density of states at fixed in-plane wave vector [32, 33]. Notice that the mode Q-factor can be obtained as $Q = \omega/[2\,\mathrm{Im}(\omega)]$.

As an example of photonic mode dispersion, in Fig. 1 we show the photonic bands of a triangular lattice of air holes in a membrane with the dielectric constant of GaAs at optical frequencies, along the Γ–M and Γ–K symmetry directions of the 2D Brillouin zone. In Fig. 1(a) a schematic picture of the structure and a definition of its direct and reciprocal lattices is displayed. A high-index membrane supports both guided modes (lying between the cladding and core light lines) and quasi-guided modes (lying above the air light line). It should be noted that the photonic band dispersion is calculated assuming the low temperature value at 1.48 eV for the dielectric constant of the GaAs layer, i.e., $\varepsilon = 12.95$. Although the band dispersion in Fig. 1(b) is calculated with a frequency-independent dielectric constant, an exciton level at $E_{\text{exc}} = 1.48$ eV (corresponding to a low-temperature exciton in a typical InGaAs quantum well) is also shown. This will be useful for the study of radiation−matter interaction in the next Section. It can be seen that the exciton energy crosses several photonic modes of the 2D photonic lattice. Only even modes with respect to the horizontal midplane (indicated with $\sigma_{xy} = +1$) are considered here.

An expanded plot of the dispersion and the mode linewidths (twice the imaginary parts of the energies) along the main symmetry directions is shown in Fig. 2. Along the ΓM orientation, mode 2 has vanishing radiative linewidth when crossing the light line and becoming a truly guided mode, while mode 1 has vanishing linewidth on approaching the Γ point. The latter behavior is determined by symmetry considerations [15, 33] since at Γ only dipole-active, twofold-degenerate modes are coupled

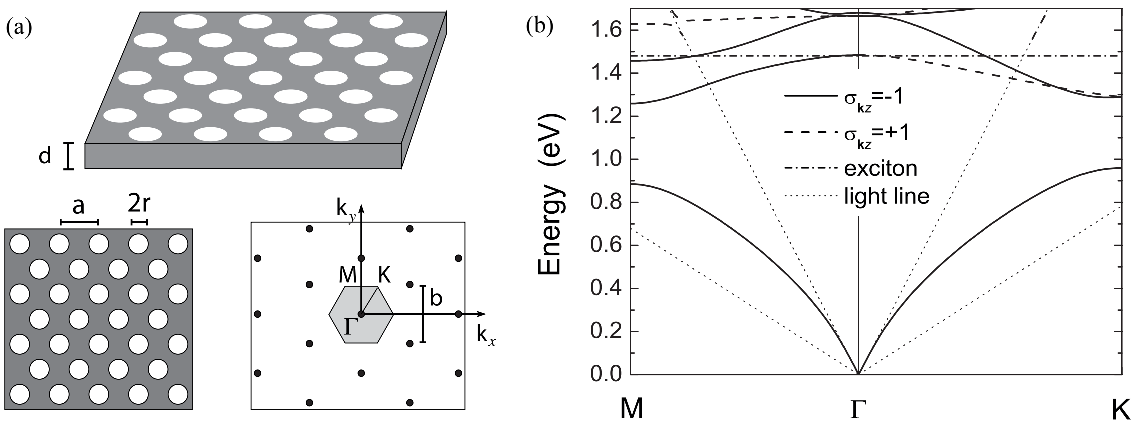

Fig. 1 (a) Schematic picture of a high index PhC membrane of thickness d patterned with a triangular lattice of air holes, together with its direct and reciprocal lattices; (b) photonic band dispersion for the structure in (a) with the following parameters: dielectric constant $\varepsilon = 12.95$, lattice constant $a = 350$ nm, membrane thickness $d = 0.4a$, hole radius $r = 0.3a$. The fundamental exciton level at 1.48 eV is also plotted. Only even modes with respect to the horizontal midplane ($\sigma_{xy} = +1$) are shown, and for each symmetry direction the modes are classified as odd ($\sigma_{kz} = -1$) or even ($\sigma_{kz} = +1$) with respect to the corresponding vertical plane of incidence. The dotted lines represent the light dispersion in the air claddings and in the effective waveguide core.

© 2005 WILEY-VCH Verlag GmbH & Co. KGaA, Weinheim

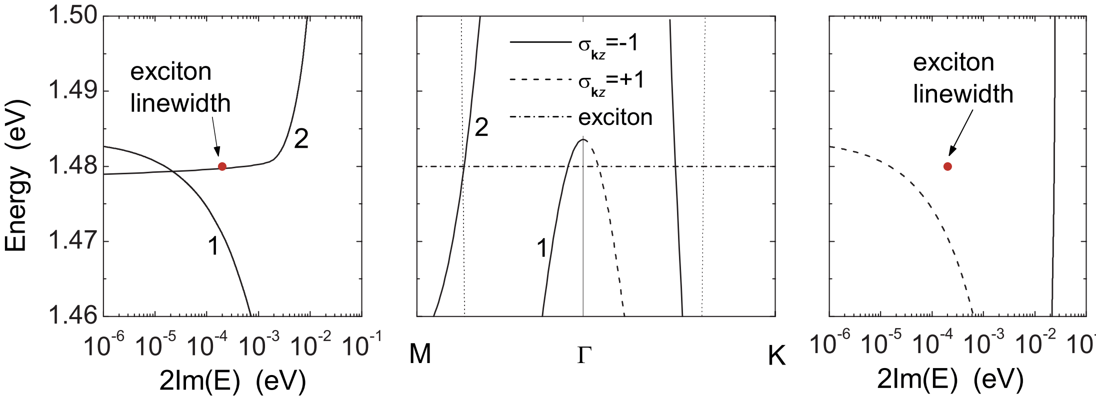

Fig. 2 (online colour at: www.pss-b.com) Complex energy dispersion of $\sigma_{xy} = +1$ photon modes for energies around the excitonic resonance, along the main symmetry directions of the triangular lattice (parameters as in Fig. 1). Left: mode linewidths along ΓM. Middle: real part of mode energies. Right: mode linewidths along ΓK. The points corresponding to a non-dispersive exciton resonance with $E_{\text{exc}} = 1.48$ eV and linewidth $\Gamma_{\text{exc}} = 2 \times 10^{-4}$ eV are also shown.

to normally incident light. Considering now the ΓK direction, the two photonic modes have different symmetries with respect to the corresponding vertical plane of incidence. In particular, the even mode (indicated with $\sigma_{kz} = +1$) has vanishing linewidth on approaching the Γ point, like the corresponding mode along ΓM. On the contrary, the odd mode ($\sigma_{kz} = -1$) has much higher radiation linewidths ($2\,\mathrm{Im}(E) > 20$ meV). The value of the photonic mode (and exciton) linewidth is a crucial parameter when considering the interaction between photon and exciton states, as discussed in the next section.

It is important to notice, in the left panel of Fig. 2, that in correspondence to the exciton resonance both photonic eigenmodes have very small linewidths ($2\,\mathrm{Im}(E) < 10^{-3}$ eV). We thus reasonably expect that photonic crystal polaritons should form at two different points in the irreducible Brillouin zone along ΓM, with two distinct anticrossings between exciton center-of-mass levels and photonic bands.

3 Exciton-polaritons in photonic crystal slabs

In order to develop a quantum-mechanical theory of polaritons in PhC slabs, we have to quantize both the photon and exciton states in the dielectric structure (a detailed account of the formalism is presented in Ref. [34]). The electric and magnetic fields are expanded as

$$\boldsymbol{E}(\boldsymbol{r}, t) = \sum_{\mu} \left(\frac{2\pi\hbar\omega_{\mu}}{4\pi\varepsilon_0 V} \right)^{1/2} \left[\hat{a}_{\mu} \boldsymbol{E}_{\mu}(\boldsymbol{r})\, \mathrm{e}^{-i\omega_{\mu} t} + \hat{a}_{\mu}^{\dagger} \boldsymbol{E}_{\mu}^{*}(\boldsymbol{r})\, \mathrm{e}^{i\omega_{\mu} t} \right], \tag{5}$$

$$\boldsymbol{H}(\boldsymbol{r}, t) = \sum_{\mu} \left(\frac{2\pi\hbar\omega_{\mu}}{4\pi\varepsilon_0 V} \right)^{1/2} \left[\hat{a}_{\mu} \boldsymbol{H}_{\mu}(\boldsymbol{r})\, \mathrm{e}^{-i\omega_{\mu} t} + \hat{a}_{\mu}^{\dagger} \boldsymbol{H}_{\mu}^{*}(\boldsymbol{r})\, \mathrm{e}^{i\omega_{\mu} t} \right], \tag{6}$$

where $\hat{a}_{\mu}^{\dagger}$ ($\hat{a}_{\mu}$) are creation (destruction) operators of field quanta with energies ω_{μ}. In the above formulas, ε_0 is the vacuum permittivity, V is a quantization volume, and $\mu = (\boldsymbol{k}, n)$ is a combined index which includes the Bloch vector $\boldsymbol{k}$ and the photonic band index n. The field eigenmodes $\boldsymbol{E}_{\mu}(\boldsymbol{r})$, $\boldsymbol{H}_{\mu}(\boldsymbol{r})$ can be calculated by solving the classical Maxwell equations and are normalized as

$$\int_V \varepsilon(\boldsymbol{r})\, \boldsymbol{E}_{\mu}(\boldsymbol{r})\, \boldsymbol{E}_{\mu'}^{*}(\boldsymbol{r})\, \mathrm{d}\boldsymbol{r} = \delta_{\mu\mu'} \,, \tag{7}$$

$$\int_V \boldsymbol{H}_{\mu}(\boldsymbol{r})\, \boldsymbol{H}_{\mu'}^{*}(\boldsymbol{r})\, \mathrm{d}\boldsymbol{r} = \delta_{\mu\mu'} \,. \tag{8}$$

© 2005 WILEY-VCH Verlag GmbH & Co. KGaA, Weinheim

For the exciton part, we consider a membrane containing a thin QW layer that is also patterned with air holes, assume strong electron–hole confinement leading to separability of the exciton wavefunction, and solve the Schrödinger equation for the center-of-mass motion in the QW plane

$$\left[-\frac{\hbar^2\nabla_\parallel^2}{2M_{\text{exc}}}+V(\boldsymbol{r}_\parallel)\right]F_{\text{cm}}(\boldsymbol{r}_\parallel)=\hbar\Omega\,F_{\text{cm}}(\boldsymbol{r}_\parallel)\,, \tag{9}$$

where $\boldsymbol{r}_\parallel=(x,y)$ and the effective potential $V(\boldsymbol{r}_\parallel)=\infty$ in air regions, while $V(\boldsymbol{r}_\parallel)=0$ in the non-patterned regions of the quantum well. We neglect dead-layer effects (the thickness of the dead layer is usually less than 10 nm, i.e., much smaller than the length scale of the photonic structure) and also image-charge potentials. Equation (9) is solved numerically by plane wave expansion, yielding quantized center-of-mass levels in the periodic potential. By this procedure, the exciton levels are labelled by the same quantum number of the electromagnetic modes: i.e., by a Bloch vector $\boldsymbol{K}_{\text{exc}}$ and a discrete index ν. This allows introducing exciton creation (destruction) operators $\hat{b}_\sigma^\dagger$ ($\hat{b}_\sigma$) corresponding to the energies $\hbar\Omega_\sigma$, where $\sigma=(\boldsymbol{K}_{\text{exc}},\nu)$ is again a combined index.

In the interaction with photon states, the Bloch vector is conserved, or $\boldsymbol{K}_{\text{exc}}\simeq\boldsymbol{k}$. However, a photonic mode with band index n couples to exciton center-of-mass levels with any ν. The interaction is determined by a matrix element of the full Hamiltonian, as first shown in Refs. [1, 2] for bulk exciton–polaritons and later extended to quantum-confined systems [3–5]. The coupling matrix element between exciton and photon takes the form

$$C_{\boldsymbol{k}n\nu}=\left(\frac{2\pi e^2\hbar\Omega_{\boldsymbol{k}\nu}^2}{4\pi\varepsilon_0\omega_{\boldsymbol{k}n}}\right)^{1/2}\langle\Psi_{\boldsymbol{k}\nu}^{(\text{exc})}|\sum_j\boldsymbol{E}_{\boldsymbol{k}n}(\boldsymbol{r}_j)\cdot\boldsymbol{r}_j|0\rangle\,, \tag{10}$$

where $\Psi_{\boldsymbol{k}\nu}^{(\text{exc})}$ is the exciton wavefunction, and the sum is over all the electrons in the QW material. If the QW exciton is a heavy-hole state, only the in-plane components of the electric field are involved and $\sigma_{xy}=+1$ modes (often called TE-like modes in the literature) are preferentially coupled. The integral can be expressed in terms the oscillator strength f of the excitonic transition, which is generally defined as

$$f=\frac{2m\omega}{\hbar}\left|\langle\Psi_{\boldsymbol{k}\nu}^{(\text{exc})}|\,\hat{\boldsymbol{e}}\cdot\sum_j\boldsymbol{r}_j|0\rangle\right|^2=\frac{2}{m\hbar\omega}\left|\langle\Psi_{\boldsymbol{k}\nu}^{(\text{exc})}|\,\hat{\boldsymbol{e}}\cdot\sum_j\boldsymbol{p}_j|0\rangle\right|^2\,, \tag{11}$$

where m is the free-electron mass, $\hat{\boldsymbol{e}}$ is the polarization unit vector of the exciton and $\boldsymbol{r}_j$ ($\boldsymbol{p}_j$) is the position (momentum) operator of the QW electrons. The matrix element (10) is found to depend on the oscillator strength per unit area, f/S, as well as on the spatial overlap between the exciton center-of-mass wavefunction and the mode electric field in the QW plane:

$$C_{\boldsymbol{k}n\nu}\simeq\left(\frac{\pi e^2\hbar^2}{4\pi\varepsilon_0 m}\,\frac{f}{S}\right)^{1/2}\int\hat{\boldsymbol{e}}\cdot\boldsymbol{E}_{\boldsymbol{k}n}(\boldsymbol{r}_\parallel,z_{\text{QW}})\,F_{\text{cm}}(\boldsymbol{r}_\parallel)\,\mathrm{d}\boldsymbol{r}_\parallel\,. \tag{12}$$

The full quantum Hamiltonian describing coupled photon and exciton states is finally given by

$$\begin{aligned}\hat{H}=&\sum_{\boldsymbol{k},n}\hbar\omega_{\boldsymbol{k}n}\hat{a}_{\boldsymbol{k}n}^\dagger\hat{a}_{\boldsymbol{k}n}+\sum_{\boldsymbol{k},\nu}\hbar\Omega_{\boldsymbol{k}\nu}\hat{b}_{\boldsymbol{k}\nu}^\dagger\hat{b}_{\boldsymbol{k}\nu}+i\sum_{\boldsymbol{k},n,\nu}C_{\boldsymbol{k}n\nu}(\hat{a}_{\boldsymbol{k}n}+\hat{a}_{-\boldsymbol{k}n}^\dagger)(\hat{b}_{\boldsymbol{k}\nu}^\dagger-\hat{b}_{-\boldsymbol{k}\nu})\\&+\sum_{\boldsymbol{k},\nu}\sum_{n_1,n_2}\frac{C_{\boldsymbol{k}n_1\nu}^*C_{\boldsymbol{k}n_2\nu}}{\hbar\Omega_{\boldsymbol{k}\nu}}(\hat{a}_{-\boldsymbol{k}n_1}+\hat{a}_{\boldsymbol{k}n_1}^\dagger)(\hat{a}_{\boldsymbol{k}n2}+\hat{a}_{-\boldsymbol{k}n_2}^\dagger)\,.\end{aligned} \tag{13}$$

It should be noticed that both photon and exciton energies are taken to be complex quantities: i.e., the imaginary part of the frequency for quasi-guided photonic modes, as well as the exciton linewidth arising from non-radiative processes, are included in the calculation. Hamiltonian (13) is diagonalized by using a generalized Hopfield transformation [1, 35] to expand new destruction (creation) operators $\hat{P}_{\boldsymbol{k}}$ ($\hat{P}_{\boldsymbol{k}}^\dagger$) as linear combinations of $\hat{a}_{\boldsymbol{k}n}$ ($\hat{a}_{\boldsymbol{k}n}^\dagger$) and $\hat{b}_{\boldsymbol{k}\nu}$ ($\hat{b}_{\boldsymbol{k}\nu}^\dagger$), with the condition $[\hat{P}_{\boldsymbol{k}},\hat{H}]=E_{\boldsymbol{k}}\hat{P}_{\boldsymbol{k}}$. The transformation,

© 2005 WILEY-VCH Verlag GmbH & Co. KGaA, Weinheim

which leads to a non-hermitian eigenvalue problem, applies also to a Hamiltonian that includes dissipative terms. The new eigenenergies $E_{\boldsymbol{k}}$ correspond to mixed excitations of radiation and matter, which can be either in a weak or in a strong-coupling regime: in the latter case they give rise to *photonic crystal polaritons*.

For a GaAs membrane containing a typical InGaAs/GaAs quantum well at the field antinode, the coupling matrix element is calculated to be of the order of 6 meV in the present structure. The exciton linewidth in high-quality structures at low temperature can be made lower than 0.6 meV [36], i.e., negligibly small as compared to the energy scale of the interaction. Thus, the eventual regime of the exciton–photon coupling depends critically on the value of the photonic mode linewidth. If the exciton interacts with a truly-guided mode, the (intrinsic) linewidth is zero and the exciton–light coupling is always in a strong-coupling regime. The resulting polaritons are evanescent and non-radiative, as they lie below the air light line. Radiative polariton states are obtained when the exciton interacts with a quasi-guided mode whose linewidth is smaller than the exciton–photon coupling. Several possible situations for the interaction of the exciton with quasi-guided modes are illustrated in Fig. 2 above.

Radiative polaritons in PhC slabs can be probed by reflectance (or transmittance) from the slab surface, as done in a pioneering paper where the strong exciton resonance of an organic molecule [bis-(phenethyl-ammonium) tetraiodoplumbate (PEPI)] with a giant oscillator strength per unit area was employed to observe the strong-coupling at room temperature [22]. Observing the same effect in III–V semiconductors is more difficult and has not been achieved at time of writing. Here we calculate the angle-resolved reflectance from the surface of the PhC slab using the scattering-matrix method [37, 38], which yields an exact numerical solution of Maxwell equations for a stratified medium consisting of patterned layers that are homogeneous in the *z*-direction. The presence of the exciton resonance is taken into account at a semiclassical level by adding a Lorentz-oscillator term to the dielectric function in the QW layers:

$$\varepsilon_{\mathrm{exc}}(\omega) = \varepsilon_{\infty}\left(1 + \frac{\hbar\omega_{\mathrm{LT}}}{\hbar(\Omega_{\mathrm{exc}} - \omega) - i\Gamma_{\mathrm{exc}}/2}\right), \tag{14}$$

where ε_{∞} is the background dielectric constant of the QW material, ω_{LT} is the longitudinal–transverse (LT) splitting and $\hbar\Omega_{\mathrm{exc}}$, Γ_{exc} are the bare exciton energy and linewidth as in the quantum calculation. The LT splitting may be related to the quantum-mechanical oscillator strength per unit area by

$$\hbar\omega_{\mathrm{LT}} = \frac{2\pi\hbar e^2}{4\pi\varepsilon_0\varepsilon_{\infty} m\Omega_{\mathrm{exc}} L_{\mathrm{QW}}}\frac{f}{S}, \tag{15}$$

where L_{QW} is the QW width. This relation is valid for a single quantum well in the strong (electron–hole) confinement regime. A fuller discussion of the relation between semiclassical and quantum descriptions of the light–exciton interaction can be found elsewhere [3–5].

In Fig. 3 we show a comparison between quantum and semiclassical treatments of PhC polaritons (results for 1D photonic lattices were previously presented in Ref. [39]), for a structure containing two InGaAs QWs. In order to make the quantum and semiclassical calculations consistent with each other, an oscillator strength per unit area $f/S = 4.2 \times 10^{12}$ cm^{-2} is assumed for each InGaAs QW, corresponding to a quantum well of width $L_{\mathrm{QW}} = 8$ nm and a LT splitting $\hbar\omega_{\mathrm{LT}} = 0.2$ meV in the semiclassical calculation. Panels (a), (c) display angle-resolved reflectance spectra along the Γ–M and Γ–K orientations, respectively, while panel (b) reports the dispersion of coupled exciton-photon modes as calculated from the quantum theory (small circles) and extracted from the spectral structures in reflectance taking into account parallel momentum conservation (square points). Along the Γ–M orientation (TE polarization of incident light) there are two anticrossing points, i.e., exciton–light coupling is in a strong-coupling regime for both photonic modes 1 and 2 previously shown in Fig. 2. Along the Γ–K orientation (TM incident polarization) there is only one anticrossing point. It is worth noting that odd modes ($\sigma_{kz} = -1$) are excited by TE incident radiation along ΓK, whilst even modes ($\sigma_{kz} = +1$) are excited by TM incident beams along ΓM. The results of Fig. 3 demonstrate that radiative polaritons can be observed by

© 2005 WILEY-VCH Verlag GmbH & Co. KGaA, Weinheim

Feature
Article

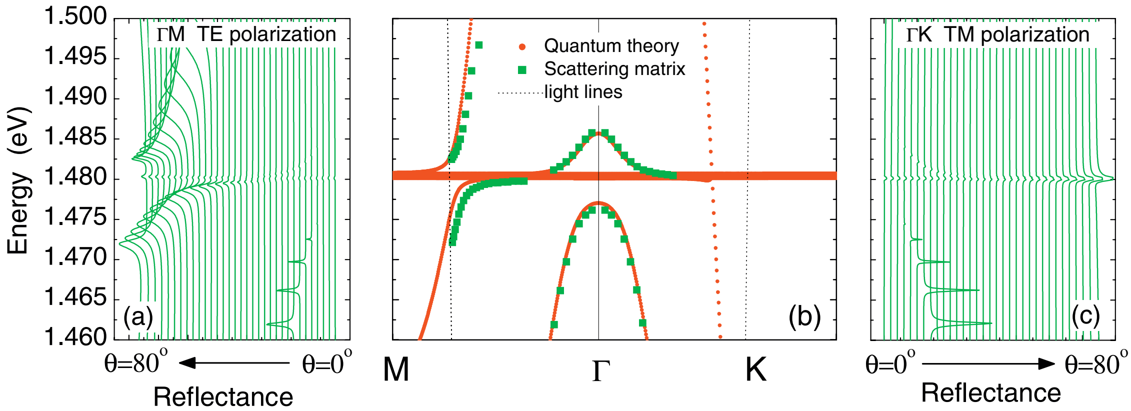

Fig. 3 (online colour at: www.pss-b.com) Photonic crystal polaritons in a 2D triangular lattice along the main symmetry directions (parameters as in Fig. 1). Scattering matrix calculations of reflectance spectra along (a) ΓM (TE incident light) and (c) ΓK (TM incident light) are compared to quantum calculations of mode dispersion in (b): small circles are from the quantum theory results, while square points are extracted from reflectance spectra in (a) and (c).

angle-resolved reflectance, provided the photonic mode linewidth (and, of course, the exciton linewidth) be smaller than the exciton–photon coupling. They also demonstrate that the semiclassical and quantum treatments of photonic-crystal polaritons yield results that are in very good agreement with each other – the expected results for *linear* optical properties.

Notice that the polariton splitting at resonance is of the order of 10 meV with two embedded QWs. This is larger than common values for III–V microcavities which are typically of the order of 4 meV with two QWs [40], and no larger than 6–8 meV even with several quantum wells close to the field antinodes [7–9]. This increase of the polariton splitting has little to do with the x, y dependence of the electric field and of the exciton envelope function: since the exciton center-of-mass levels are nearly degenerate, for a given photonic mode there is always a linear combination of exciton states which has the proper spatial dependence to yield an overlap matrix element (10) close to unity. In this respect, the physics of exciton-light coupling in photonic crystals is similar to the case of pillar microcavities [35] where a cavity mode couples to several exciton states and the polariton splitting has only a slight dependence on the pillar radius. The reason for the increased polariton splitting in PhCs lies in a better field confinement along the vertical direction: in a microcavity with dielectric mirrors the penetration of the electric field in the distributed Bragg reflectors reduces the overlap of the cavity mode with the exciton state [5, 40], while in a PhC slab the fundamental waveguide mode is almost perfectly confined within the slab, thus yielding optimal coupling with the QW exciton.

4 Nanoscale cavities in photonic crystal slabs

Point defects in PhC slabs behave as 0D cavities and support localized modes in the photonic gap. Cavity modes are always subject to radiation losses, as they have no wave vector and are coupled to the continuum of leaky slab modes by the dielectric modulation. Still, photonic cavities with large quality factor Q and small mode volumes can be defined. The quality factor can be increased by a momentum-space design, which allows to reduce the radiative component of the confined photonic mode [41]. In real space, this corresponds to changes of the position or size of the nearby holes. One of the best performing cavity structures consists of three missing holes along the ΓK direction of the triangular lattice: by using the principle of "gentle confinement", which consists of shifting the positions of the holes close to the defect, Q-factors as high as 1.5×10^5 have been demonstrated [42]. The very high Q-factors can also be interpreted with a Fabry–Pérot model [43]. Using a conceptually different design approach, based on PhC slab heterostructures with varying lattice constants, measured Q-factors of the order of 6×10^5 have been reported [44].

© 2005 WILEY-VCH Verlag GmbH & Co. KGaA, Weinheim

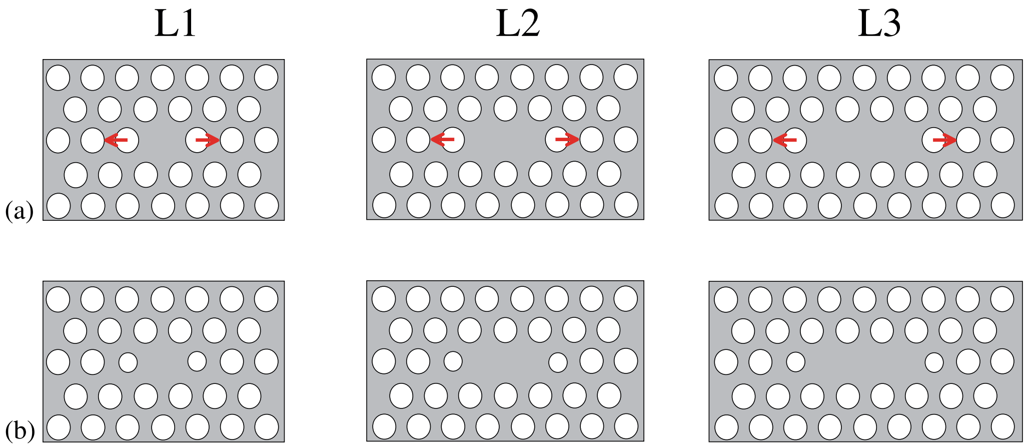

Fig. 4 (online colour at: www.pss-b.com) Schematic structure of L1, L2, L3 point defects with (a) hole displacement and (b) hole shrinking.

Within the present method, the quality factor is calculated as $Q = \omega/[2\,\mathrm{Im}(\omega)]$ by introducing a supercell in two directions and evaluating $\mathrm{Im}(\omega)$ in perturbation theory with the use of Eq. (4). Notice that by using a supercell, all photonic modes that fall above the light line upon folding in a reduced Brillouin zone become radiative: by this procedure, the determination of the Q-factor of cavity modes is similar to the calculation of propagation losses of extended modes. We focus on cavities with one, two or three missing holes in the triangular lattice (L1, L2, L3 defect) and consider a displacement or a shift of the nearby holes in ΓK direction, as illustrated in Fig. 4. We calculate only intrinsic losses, i.e., we do not include the effect of disorder which is left for further analysis.

In Fig. 5 we show the quality factor as a function of (a) hole displacement and (b) hole shrinking. All curves have a pronounced maximum, confirming that the Q-factor is indeed increased by gentle confinement. For the case of the L3 defect with hole displacement, we find $Q = 4.5 \times 10^4$ for $\Delta x/a = 0.15$, in agreement with the experimental results [18] obtained on nanocavities in Silicon membranes with a cavity mode around $\lambda = 1.55\,\mu\mathrm{m}$. The maximum calculated value is $Q \simeq 1.5 \times 10^5$ at $\Delta x/a = 0.18$. The experimental values for $\Delta x/a = 0.2$ and 0.25 are lower than the theoretical ones. Turning now to the case of hole shrinking, we notice that the maximum of the Q-factor as a function of $\Delta r/a$ is broader, implying that the structure may be more tolerant to small imperfections in fabrication. When the two nearby holes are shrunk to zero radius, the curve relative to the Ln defect tends to the value for the L(n +2) defect at

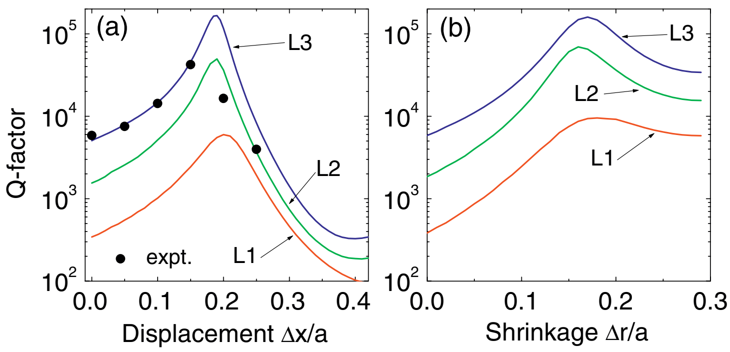

Fig. 5 (online colour at: www.pss-b.com) Quality factor for L1, L2, L3 defects in a silicon membrane with $\varepsilon_r = 12$, $a = 420$ nm, $d/a = 0.6$, $r/a = 0.29$ as a function of (a) displacement and (b) shrinking of the two holes close to the point defect along the ΓK direction. The experimental points are taken from Ref. [18]. The mode considered has symmetry $\sigma_{xy} = +1$.

© 2005 WILEY-VCH Verlag GmbH & Co. KGaA, Weinheim

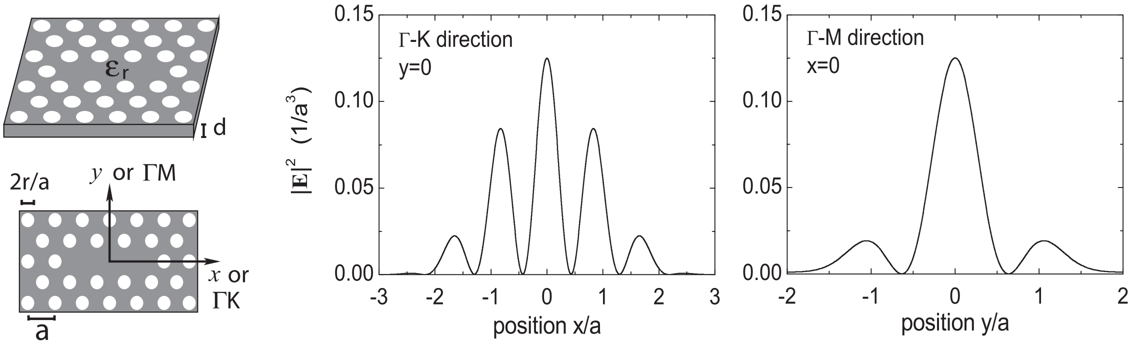

Fig. 6 Schematice picture of a L3 nanocavity and field profile of the ground cavity mode along the Γ–K and Γ–M symmetry directions for structure parameters as in Fig. 5. The field is calculated for the structure with no shift or shrinking of nearby holes.

$\Delta r = 0$. The results of Fig. 5 show clearly that an L3 cavity with optimal hole displacement or shrinking (maximum of L3 curves) has a higher Q than a bare L5 cavity (end point of L3 curve in Fig. 5b).

In Fig. 6 we show the electric field profile along the main symmetry directions for the ground mode of the L3 cavity (for null displacement and shrinking of nearby holes). The square modulus of the electric field has a maximum at the cavity center, but it oscillates along the Γ–K direction (and, to a lesser extent, along the Γ–M direction) with secondary maxima. The oscillations along Γ–K result from the physical origin of the L3 cavity mode, which results from quantization of the line-defect mode corresponding to a missing row of holes along the Γ–K direction or $W1$ *waveguide* [45]: the quantized wave vector in the extended zone scheme is of the order of $4\pi/(3a)$, which explains the period of the oscillations. Figure 6 implies that there are three favorable positions for placing a dipole emitter at field antinodes: however, the extension of the region where the field is close to its maximum value is of the order of $\pm 0.1a$, i.e., much smaller than the lattice constant. From Fig. 6 it is also possible to deduce the *mode volume*, which is generally defined as [46, 47]

$$\widetilde{V} = \frac{\int \varepsilon(\boldsymbol{r})\, |\boldsymbol{E}(\boldsymbol{r})|^2 \, \mathrm{d}\boldsymbol{r}}{\varepsilon(\boldsymbol{r}_{\text{peak}})\, |\boldsymbol{E}(\boldsymbol{r}_{\text{peak}})|^2}\,, \tag{16}$$

where $\boldsymbol{r}_{\text{peak}}$ is the peak position of the product $\varepsilon(\boldsymbol{r})\,|\boldsymbol{E}(\boldsymbol{r})|^2$ and the integral is the normalization of the electric field. The mode volume for the field shown in Fig. 6 is $\widetilde{V} = (\varepsilon_r |\boldsymbol{E}(\boldsymbol{r}_{\text{peak}})|^2)^{-1} \simeq 0.67a^3$, where the electric field is normalized according to Eq. (7), and since the dimensionless frequency of the cavity mode is $a/\lambda \simeq 0.27$ we get $\widetilde{V} \simeq 0.56(\lambda/n_r)^3$ ($n_r = \sqrt{\varepsilon_r}$ is the dielectric constant at the peak position). The mode volume of this kind of PhC nanocavity is smaller than a wavelength cubed, i.e., the electromagnetic field is very well confined in all three spatial directions.

5 Strong exciton-light coupling in nanocavities

In this section we consider a single InAs quantum dot (QD) coupled to a PhC nanocavity realized in a GaAs membrane. While quantum-well excitons are described by bosonic operators, the exciton transition in a single quantum dot can be modelled to a first approximation by a two-level system. The theory of radiation-matter coupling in this case relies on the Jaynes–Cummings model. If the QD interacts with a single cavity mode, the Hamiltonian is

$$H = \hbar\Omega_{\text{exc}}\hat{\sigma}_3 + \hbar\omega_\mu(\hat{a}_\mu^\dagger \hat{a}_\mu + \tfrac{1}{2}) + i\hbar\Omega_0(\hat{\sigma}_- \hat{a}_\mu^\dagger - \hat{\sigma}_+ \hat{a}_\mu)\,, \tag{17}$$

© 2005 WILEY-VCH Verlag GmbH & Co. KGaA, Weinheim

where $\Omega_{\rm exc}$ is the fundamental exciton frequency, $\hat{\sigma}_+$, $\hat{\sigma}_-$, $\hat{\sigma}_3$ are pseudo-spin operators for the two-level system with ground (excited) state $|g\rangle$ ($|e\rangle$) and $a_\mu^\dagger, a_\mu$ are creation/destruction operators for the cavity mode μ. The coupling constant $\Omega_0 = \langle \boldsymbol{d}\cdot\boldsymbol{E}\rangle/\hbar$ of the quantum dot−cavity interaction is

$$\Omega_0 = \left(\frac{1}{4\pi\varepsilon_0}\,\frac{\pi e^2 f}{\varepsilon_r m \tilde{V}_\mu}\right)^{1/2}, \tag{18}$$

where f is the oscillator strength of the transition, $\tilde{V}_\mu$ is the mode volume defined in Eq. (16), ε_r (ε_0) is the relative (vacuum) permittivity and m is the free-electron mass. We are assuming that the quantum dot is located at the peak position of the electric field. The condition of spatial overlap between the QD and the cavity mode can be met by aligning the cavity around a chosen quantum dot, as demonstrated in Refs. [48–50].

The quantum Hamiltonian (17) has a discrete spectrum consisting in a ladder of dressed states, in which each excited state is split into two levels separated by $2\hbar\Omega_0\sqrt{n+1}$, where n is the number of photons in the cavity mode [51]. In the weak excitation regime, we can consider only the transition between the ground state and the first excited doublet, whose splitting $2\hbar\Omega_0$ corresponds to the vacuum-field Rabi splitting between the QD transition and the single cavity mode. In order to take into account the finite linewidth of both the QD exciton ($\Gamma_{\rm exc}$) and the cavity mode ($2\,{\rm Im}(\hbar\omega_\mu) = \hbar\omega_\mu/Q_\mu$), a master-equation approach has been used, which allows calculating the spontaneous emission spectrum. This leads to an analytical expression for the complex energy splitting of the two oscillators [52, 53]

$$\hbar\Omega_\pm = \hbar\Omega_{\rm exc} \pm \sqrt{\hbar^2\Omega_0^2 - \left(\frac{\Gamma_{\rm exc} - (\hbar\omega_\mu/Q)}{4}\right)^2} - i\left(\frac{\Gamma_{\rm exc} + (\hbar\omega_\mu/Q)}{4}\right). \tag{19}$$

We assume the quantum dot to be in resonance with the cavity mode, i.e., the QD has to be not only *spatially* but also *spectrally* resonant. Achieving spectral overlap is made difficult by the size distribution of self-assembled QDs. Spectral resonance is imposed here by properly designing the GaAs PhC nanocavity to have the ground cavity mode at energy $\hbar\omega_\mu \sim 1.3$ eV ($\lambda_\mu \sim 950$ nm), which is a typical value for the fundamental exciton resonance of InAs QDs.

The solutions of Eq. (19) are plotted in Fig. 7 as a function of the Q-factor. We take a mode volume $\tilde{V} \simeq 1.1\times10^{-14}$ cm^3, estimated from $\sim 0.56(\lambda/n_r)^3$ at a wavelength $\lambda = 950$ nm and $n_r = \sqrt{\varepsilon_r} \simeq 3.54$ (low temperature value for GaAs at 1.3 eV). The oscillator strength $f \simeq 10.7$ is a typical value for self-assembled InAs QDs corresponding to the measured lifetime $\tau \sim 1$ ns [10]. The crossover from weak to strong coupling is seen to appear at $Q \sim 2000$, even if the corresponding imaginary part is still larger than the Rabi splitting. The maximum Rabi splitting for this kind of systems is seen to be reached already for $Q \sim 10\,000$. Such values of Q are well within the reach of present-day fabrication technology, even for

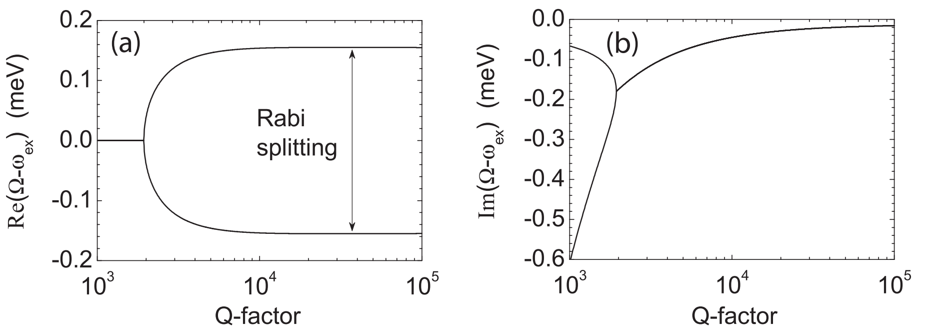

Fig. 7 (a) Real and (b) imaginary parts of Eq. (19) as a function of Q-factor, for QD parameters $\Gamma_{\rm exc} = 0.05$ meV, $f = 10.7$, and effective cavity mode volume $\tilde{V} = 1.1\times10^{-14}$ cm^3.

© 2005 WILEY-VCH Verlag GmbH & Co. KGaA, Weinheim

cavities in GaAs slabs for which the Q-factor is limited by absorption at the GaAs/native oxide interfaces at the hole sidewalls [50].

In Figs. 8(a–c) the calculated mode energy, Q-factor and effective volume are plotted as a function of the holes' shift, $\Delta x/a$, for proper design parameters of the GaAs PhC membrane. The resonance energy and the mode volume do not change appreciably, while the Q-factor has a dramatic increase with a maximum $Q > 10^5$ for $\Delta x/a \sim 0.18$. The latter results are employed to calculate the complex splitting as a function of $\Delta x/a$, which is shown in Fig. 8(d) and (e). It is evident that the system is always in the strong coupling regime, regardless of the displacement of the nearby holes. This result is in agreement with the calculations of Figs. 7, because the Q-factor is always higher than 2000 for the present nanocavity. The imaginary part of the complex splitting has a minimum for a value of $\Delta x/a$ corresponding to the maximum Q-factor. It is arguable that, in order to observe the strong coupling, shifting the holes in the PhC slab nanocavity could be of importance for reducing the emission linewidth of the two peaks. These results agree well with recent experimental findings [21] as well as with a theoretical study of the strong-coupling based on a Green's function approach [54].

Notice that the physics of the Jaynes–Cummings model (17) is very different from that of the Hamiltonian (13) describing the interaction between photonic modes and quantum-well excitons. The point is that the QW exciton is a delocalized excitation that represents a collection of excited unit cells and has a bosonic character, while the quantum-dot transition is localized and has to be modelled by a two-level system which cannot be excited more than once. The two systems behave in a similar way under weak excitation conditions, but the differences become manifest on increasing the excitation, as the quantum-dot transition coupled to the nanocavity mode gives a Rabi splitting that increases like $\sqrt{n+1}$. Indeed, the coupled QD–cavity system is expected to display a Mollow-type spectrum [55] with a classical Rabi splitting at high excitation intensity. Of course, a more complete model should take into account bi-exciton and multi-exciton states of the quantum dot [56, 57] with their complex many-body interactions.

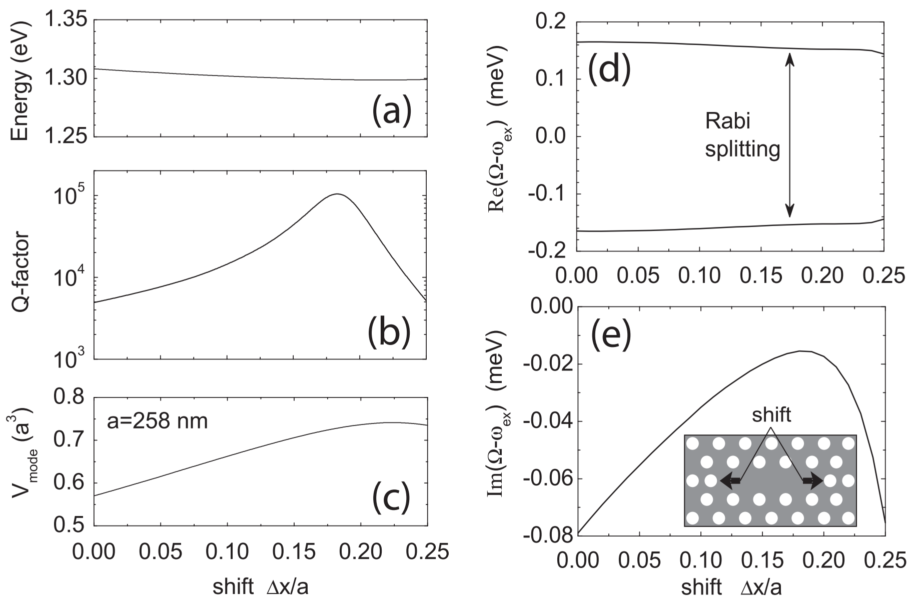

Fig. 8 Results for a PhC slab nanocavity in GaAs air bridge. Parameters of the structure are: $\varepsilon_r = 12.53$, $d = 126$ nm, $a = 258$ nm, $r/a = 0.3$. (a) Energy, (b) Q-factor, and (c) mode volume for the cavity mode as a function of the shift of two holes along the x-direction. (d) Real and (e) imaginary parts of Eq. (19), plotted as a function of the holes' shift by using the quantities calculated in (a), (b), and (c), and QD parameters $\Gamma_{\text{exc}} = 0.05$ meV, $f = 10.7$.

© 2005 WILEY-VCH Verlag GmbH & Co. KGaA, Weinheim

6 Conclusions

Photonic crystal slabs are very suitable systems for the control of light propagation and confinement in all spatial directions. A recently developed theory of photonic crystal slabs has been reviewed. The main conclusions of the present work are as follows.

Exciton-polaritons can form in PhC slabs with embedded quantum wells when a narrow excitonic transition is in resonance with either a truly-guided or a quasi-guided photonic mode: in the latter case, the intrinsic linewidths of the exciton and of the photonic mode need to be smaller than the coupling matrix elements. When these conditions are met, the polariton splitting can be larger than for polariton in microcavities, due to the tighter field confinement in a high-index planar waveguide. Polaritons arising from excitons in interaction with quasi-guided modes are radiative and can be probed by reflectance from the slab surface. The results of quantum and semiclassical treatments of photonic crystal polaritons are in very good agreement with each other.

Nanoscale cavities realized in photonic crystal slabs have very high Q-factors and low mode volumes: on these respects they are more performing than usual 3D microcavities like micro-pillars and micro-disks. On the other hand, their electric field profile is rapidly varying, making spatial alignment of a single quantum dot more difficult to achieve. Starting from a Jaynes–Cummings model for a two-level system coupled to a cavity mode, we have quantified the conditions for a single QD transition interacting with a PhC nanocavity to be in a strong-coupling regime with a vacuum-field Rabi splitting. Quality factors larger than 2000 are already sufficient to achieve strong coupling. This makes PhC nanocavities very promising systems for quantum-electrodynamics applications at a nanoscale level.

Acknowledgements This paper is dedicated to Professor Marc Ilegems on the occasion of his sixty-fifth birthday. Useful discussions with R. Ferrini, K. Hennessy and R. Houdré are gratefully acknowledged. This work was supported by the Italian Ministry for Education, University and Research (MIUR) through Cofin and FIRB programs as well as by the National Institute for the Physics of Matter (INFM) through PRA PHOTONIC.

References

[1] J. J. Hopfield, Phys. Rev. **112**, 1555 (1958).
[2] V. M. Agranovich, J. Exp. Theor. Phys. **37**, 430 (1959) [Sov. Phys. JETP **37**, 307 (1960)].
[3] L. C. Andreani, in: Confined Electrons and Photons – New Physics and Devices, edited by E. Burstein and C. Weisbuch (Plenum Press, New York, 1995), p. 57.
[4] V. Savona, in: Confined Photon Systems – Fundamentals and Applications, edited by H. Benisty, J.-M. Gérard, R. Houdré, J. Rarity, and C. Weisbuch (Springer, Berlin, 1999), p. 173.
[5] L. C. Andreani, in: Electron and Photon Confinement in Semiconductor Nanostructures, edited by B. Deveaud, A. Quattropani, and P. Schwendimann (IOS Press, Amsterdam, 2003), p. 105.
[6] C. Weisbuch, M. Nishioka, A. Ishikawa, and Y. Arakawa, Phys. Rev. Lett. **69**, 3314 (1992).
[7] R. Houdré, C. Weisbuch, R. P. Stanley, U. Oesterle, P. Pellandini, and M. Ilegems, Phys. Rev. Lett **73**, 1043 (1994).
[8] R. Houdré, R. P. Stanley, U. Oesterle, M. Ilegems, and C. Weisbuch, Phys. Rev. B **49**, 16761 (1994).
[9] M. S. Skolnick, T. A. Fisher, and D. M. Whittaker, Semicond. Sci. Technol. **13**, 645 (1998).
[10] J.-M. Gérard, B. Sermage, B. Gayral, B. Legrand, E. Costard, and V. Thierry-Mieg, Phys. Rev. Lett. **81**, 1110 (1998).
[11] J. Bloch, F. Boeuf, J.-M. Gérard, B. Legrand, J.-Y. Marzin, R. Planel, V. Thierry-Mieg, and E. Costard, Physica E **2**, 915 (1998).
[12] B. Gayral, J.-M. Gérard, B. Sermage, A. Lamaitre, and C. Dupuis, Appl. Phys. Lett. **78**, 2828 (2001).
[13] E. Yablonovitch, Phys. Rev. Lett. **58**, 2059 (1987).
[14] S. John, Phys. Rev. Lett. **58**, 2486 (1987).
[15] K. Sakoda, Optical Properties of Photonic Crystals (Springer, Berlin, 2001).
[16] S. G. Johnson and J. D. Joannopoulos, Photonic Crystals: the Road from Theory to Practice (Kluwer, Dordrecht, 2002).
[17] For recent reviews, see e.g. papers in IEEE J. Quantum Electron. **38**, Feature Section on Photonic Crystal Structures and Applications, edited by T. F. Krauss and T. Baba (2002), pp. 724–963.
[18] T. Akahane, T. Asane, B.-S. Song, and S. Noda, Nature **425**, 944 (2003).

© 2005 WILEY-VCH Verlag GmbH & Co. KGaA, Weinheim

[19] M. Notomi, A. Shinya, S. Mitsugi, E. Kuramochi, and H.-Y. Ryu, Opt. Express **12**, 1551 (2004).
[20] J. P. Reithmaier, G. Sęk, A. Löffler, C. Hofmann, S. Kuhn, S. Reitzenstein, L. V. Keldysh, V. D. Kulakovskii, T. L. Reinecke, and A. Forchel, Nature **432**, 197 (2004).
[21] T. Yoshie, A. Scherer, J. Hendrickson, G. Khitrova, H. M. Gibbs, G. Rupper, C. Ell, O. B. Shchekin, and D. G. Deppe, Nature **432**, 200 (2004).
[22] T. Fujita, Y. Sato, T. Kuitani, and T. Ishihara, Phys. Rev. B **57**, 12428 (1998).
[23] V. N. Astratov, D. M. Whittaker, I. S. Culshaw, R. M. Stevenson, M. S. Skolnick, T. F. Krauss, and R. M. De La Rue, Phys. Rev. B **60**, 16255 (1999).
[24] V. Pacradouni, W. J. Mandeville, A. R. Cowan, P. Paddon, J. F. Young, and S. R. Johnson, Phys. Rev. B **62**, 4204 (2000).
[25] M. Patrini, M. Galli, F. Marabelli, M. Agio, L. C. Andreani, D. Peyrade, and Y. Chen, IEEE J. Quantum Electron. **38**, 885 (2002).
[26] A. M. Malvezzi, G. Vecchi, M. Patrini, G. Guizzetti, L. C. Andreani, F. Romanato, L. Businaro, E. Di Fabrizio, A. Passaseo, and M. De Vittorio, Phys. Rev. B **68**, 161306 (R) (2003).
[27] J. P. Mondia, H. M. Van Driel, W. Jiang, A. R. Cowan, and J. F. Young, Opt. Lett. **28**, 2500 (2003).
[28] J. Torres, D. Coquillat, R. Legros, J. P. Lascaray, F. Teppe, D. Scalbert, D. Peyrade, Y. Chen, O. Briot, M. Le Vassor d'Yerville, E. Centeno, D. Cassagne, and J. P. Albert, Phys. Rev. B **69**, 085105 (2004).
[29] G. Vecchi, J. Torres, D. Coquillat, M. Le Vassor D'Yerville, and A. M. Malvezzi, Appl. Phys. Lett. **84**, 1245 (2004).
[30] M. Galli, M. Belotti, D. Bajoni, M. Patrini, G. Guizzetti, D. Gerace, M. Agio, L. C. Andreani, and Y. Chen, Phys. Rev. B **70**, 081307(R) (2004).
[31] L. C. Andreani and M. Agio, IEEE J. Quantum Electron. **38**, 891 (2002).
[32] T. Ochiai and K. Sakoda, Phys. Rev. B **64**, 045108 (2001).
[33] L. C. Andreani, phys. stat. sol. (b) **234**, 139 (2002).
[34] D. Gerace, Photonic Modes and Radiation–Matter Interaction in Photonic Crystal Slabs, Ph.D. thesis, University of Pavia (2004).
[35] G. Panzarini and L. C. Andreani, Phys. Rev. B **60**, 16799 (1999).
[36] L. A. Dunbar, R. P. Stanley, M. Lynch, J. Hegarty, U. Oesterle, R. Houdré, and M. Ilegems, Phys. Rev. B **66**, 195307 (2002).
[37] D. M. Whittaker and I. S. Culshaw, Phys. Rev. B **60**, 2610 (1999).
[38] A. L. Yablonskii, E. A. Muljarov, N. A. Gippius, S. G. Tikhodeev, T. Fujita, and T. Ishihara, J. Phys. Soc. Jpn. **70**, 1137 (2001).
[39] D. Gerace, M. Agio, and L. C. Andreani, phys. stat. sol. (c) **1**, 446 (2004).
[40] V. Savona, L. C. Andreani, P. Schwendimann, and A. Quattropani, Solid State Commun. **93**, 733 (1995).
[41] K. Srinivasan and O. Painter, Opt. Express **10**, 670 (2002).
[42] Y. Akahane, T. Asano, B.-S. Song, and S. Noda, Opt. Express **13**, 1202 (2005).
[43] C. Sauvan, Ph. Lalanne, and J. P. Hugonin, Phys. Rev. B **71**, 165118 (2005).
[44] B.-S. Song, S. Noda, T. Asano, and Y. Akahane, Nature Mater. **4**, 207 (2005).
[45] L. C. Andreani, D. Gerace, and M. Agio, Photon. Nanostruct. **2**, 103 (2004).
[46] O. Painter, R. K. Lee, A. Scherer, A. Yariv, J. D. O'Brien, P. D. Dapkus, and I. Kim, Science **284**, 1819 (1999).
[47] S. T. Ho, L. Wang, and S. Park, in: Confined Photon Systems – Fundamentals and Applications, edited by H. Benisty, J.-M. Gérard, R. Houdré, J. Rarity, and C. Weisbuch (Springer, Berlin, 1999), p. 243.
[48] K. Hennessy, C. Reese, A. Badolato, C. F. Wang, A. Imamoğlu, P. M. Petroff, E. Hu, G. Jin, S. Shi, and D. W. Prather, Appl. Phys. Lett. **83**, 3650 (2003).
[49] K. Hennessy, A. Badolato, P. M. Petroff, and E. Hu, Photon. Nanostruct. **2**, 65 (2004).
[50] A. Badolato, K. Hennessy, M. Atatüre, J. Dreiser, E. Hu, P. M. Petroff, and A. Imamoğlu, Science **308**, 1158 (2005).
[51] S. Haroche in: Fundamental Systems in Quantum Optics, edited by J. Dalibard, J. M. Raimond, and J. Zinn-Justin (Elsevier, Amsterdam, 1992).
[52] H. J. Carmichael, R. J. Brecha, M. G. Raizen, H. J. Kimble, and P. R. Rice, Phys. Rev. A **40**, 5516 (1989).
[53] L. C. Andreani, G. Panzarini, and J.-M. Gérard, Phys. Rev. B **60**, 13276 (1999).
[54] S. Hughes and H. Kamada, Phys. Rev. B **70**, 195313 (2004).
[55] B. R. Mollow, Phys. Rev. **188**, 1969 (1969).
[56] E. Moreau, I. Robert, L. Manin, V. Thierry-Mieg, J.-M. Gérard, and I. Abram, Phys. Rev. Lett. **87**, 183601 (2001).
[57] D. V. Regelman, U. Mizrahi, D. Gershoni, E. Ehrenfreund, W. V. Schoenfeld, and P. M. Petroff, Phys. Rev. Lett. **87**, 257401 (2001).

© 2005 WILEY-VCH Verlag GmbH & Co. KGaA, Weinheim